Multi-criteria evaluation of wheel/rail degradation at railway crossings

Wei, Zilong; Núñez, Alfredo; Liu, Xiubo; Dollevoet, Rolf; Li, Zili

DOI
10.1016/j.triboint.2019.106107

Publication date
2020

Document Version
Final published version

Published in
Tribology International

Tribology International 144 (2020) 106107

Contents lists available at ScienceDirect

Tribology International

journal homepage: http://www.elsevier.com/locate/triboint

Multi-criteria evaluation of wheel/rail degradation at railway crossings

Zilong Wei [a,b], Alfredo Núñez [b,*], Xiubo Liu [a], Rolf Dollevoet [b], Zili Li [b]

[a] Infrastructure Inspection Research Institute, China Academy of Railway Sciences Corporation Limited, China
[b] Section of Railway Engineering, Department of Engineering Structures, Faculty of Civil Engineering and Geosciences, Delft University of Technology, the Netherlands

ARTICLE INFO

Keywords:
Railway crossing
Wheel/rail degradation
Finite element modeling
Multi-criteria evaluation

ABSTRACT

This study evaluates the degradation of wheels and rails at railway crossings. The evaluation method is composed of 1) finite element simulation of dynamic wheel/crossing interaction and 2) multi-criteria analysis of wheel/rail degradation in terms of yield behavior, rolling contact fatigue (RCF) and wear. With the aid of this method, we conducted a case study identifying the proper yield strength of rail steel material for a 54E1-1:9 crossing under a specified traffic condition. The case study indicates that the wear of contact bodies is more sensitive to train speed compared with yield and RCF; the increase of rail yield strength suppresses rail degradation while exacerbating wheel degradation; and rail yield strength in the range of 500–600 MPa is preferred to achieve a good trade-off between the wheel and rail degradations.

1. Introduction

Railway crossings are important components for the railway system as they provide the flexibility to change the direction of train movement from one track to another. The design of crossings includes an inherent geometric discontinuity, which induces undesired vibrations and high wheel-rail impact forces. Subsequently, crossings are critical components that are prone to exacerbate the degradation of both wheels and rails [1,2].

In the literature, extensive efforts have been made to reduce the degradation of wheels and crossing rails, e.g., optimizing the profile [3–6], structure [7,8], and material [9–11] and modifying the friction at the wheel/rail interface [12–14]. Each of these measures holds its own advantages and limitations. For example, new track structures (e.g., under sleeper pads) are used to reduce the wheel/rail impact, yet their benefits are usually limited to certain frequency ranges [15]. Rail materials with high hardness are expected to decelerate rail degradation; however, this deceleration may speed up wheel degradation. Friction modifiers are beneficial to reduce wear and rolling contact fatigue (RCF). However, friction modifiers contribute little to reduce the wheel-rail impact force and the consequent structural vibrations. In addition, it is difficult to determine the best friction coefficient because of the complex contact behavior between wheels and crossing rails. Furthermore, it is a common practice that railway tracks and vehicles are operated by different authorities. Thus, the match between the wheel and crossing is seldom considered, leading to much faster degradation of one component than another. Therefore, it is important to investigate new methodologies capable of evaluating the integrated performance of wheels and crossing rails, considering the relevant characteristics as much as possible. This investigation would allow effective measures to be taken to slow down wheel/crossing degradation systematically, positively impacting on improving the safety of train operation and minimizing maintenance costs.

The evaluation of wheel/rail degradation requires a precise analysis of wheel/rail contact parameters such as contact force, contact stress and micro-slip. These parameters are difficult to measure in-situ, so they are often obtained using numerical simulations. In the literature, contact parameters can be estimated by means of multi-body dynamics (MBD) and finite element (FE) methods. In the MBD method, the Hertz or semi/multi-Hertz theories [16–18] are employed to obtain the normal contact solution, while the FASTSIM algorithm [19] is often used for solving the tangential contact problem. These methods are established on the half-space and linear elasticity assumption. At crossings, these methods may introduce numerical errors due to conformal contact, large variations in the contact angle and nonlinear deformation [20,21].

To overcome the limitations of MBD based methods at crossings, the FE method is employed in this study. In Refs. [22,23], a 3D FE model of a crossing was developed to investigate the dynamic wheel/rail interaction. The simulated dynamic response was verified with axle box acceleration measurements, demonstrating a good match in terms of major frequency contents and vibration energy [22]. The FE model was also

* Corresponding author.
E-mail addresses: weizilong@rails.cn (Z. Wei), A.A.NunezVicencio@tudelft.nl (A. Núñez), xbliu@rails.cn (X. Liu), R.P.B.J.Dollevoet@tudelft.nl (R. Dollevoet), Z.Li@tudelft.nl (Z. Li).

https://doi.org/10.1016/j.triboint.2019.106107
Received 22 August 2019; Received in revised form 6 December 2019; Accepted 7 December 2019
Available online 9 December 2019

Nomenclature

Symbol	Definition
d	sliding distance
F_N, F_T	wheel/rail normal and tangent contact forces
FI^n_{surf}	surface fatigue index at element n
H	material hardness
J^{YB}	objective functions for characterizing yield behavior
J^{RCF}	objective functions for characterizing RCF
J^{W}	objective functions for characterizing wear
J^{WRD}	index of wheel/rail degradation behavior
$\overline{J}$, $\underline{J}$	maximum and minimum of degradation index
$\widehat{J}$	estimated degradation index at a certain combination of scenarios
k	yield strength in shear
k_s	wear coefficient
L_m	axle load in scenario m
M_T	driving torque
N	total number of node or element
p	Pressure within contact patch
p_0	maximum pressure within contact patch
P_{F}	Pareto front
s	sliding velocity
T	duration of wheel/rail contact at a node
V_{wear}	wear volume
v_m	train speed in scenario m
X_{Pareto}	Pareto-optimal set
ΔT	time step for output
Δz^n	wear depth at node n
η	weight coefficient for a degradation type
θ	fixed parameters in evaluation
λ	variable to be evaluated
μ	friction coefficient
μ_T	traction coefficient
ξ_m	ratio of scenario m within total traffics
ξ^v_m	ratio of certain train speed over total traffics
ξ^L_m	ratio of certain axle load over total traffics
ξ^σ_m	ratio of certain wheel yield strength over total traffics
$\overline{\xi}_m$	normalized ratio of scenario m
σ^n_v	von Mises stress at element n
ω_m	combination of traffic parameters in scenario m

used to predict the degradation of crossing rails, which agreed well with in-situ 3D profile measurements and field observations [23]. In this study, the application of the FE model is extended to analyze wheel/rail degradation in terms of yield behavior, RCF and wear. Simulation results serve as inputs for a multi-criteria evaluation of the integrated performance of wheels and crossing rails. Finally, the degradation behavior between the wheels and rails can be quantified for various parameter scenarios.

The structure of this paper is as follows. Section 2 illustrates the FE modeling and the methods for analyzing wheel/rail degradation. In Section 3, multi-criteria evaluation is conducted to investigate the integrated performance of wheels and crossing rails. Section 4 conducts a

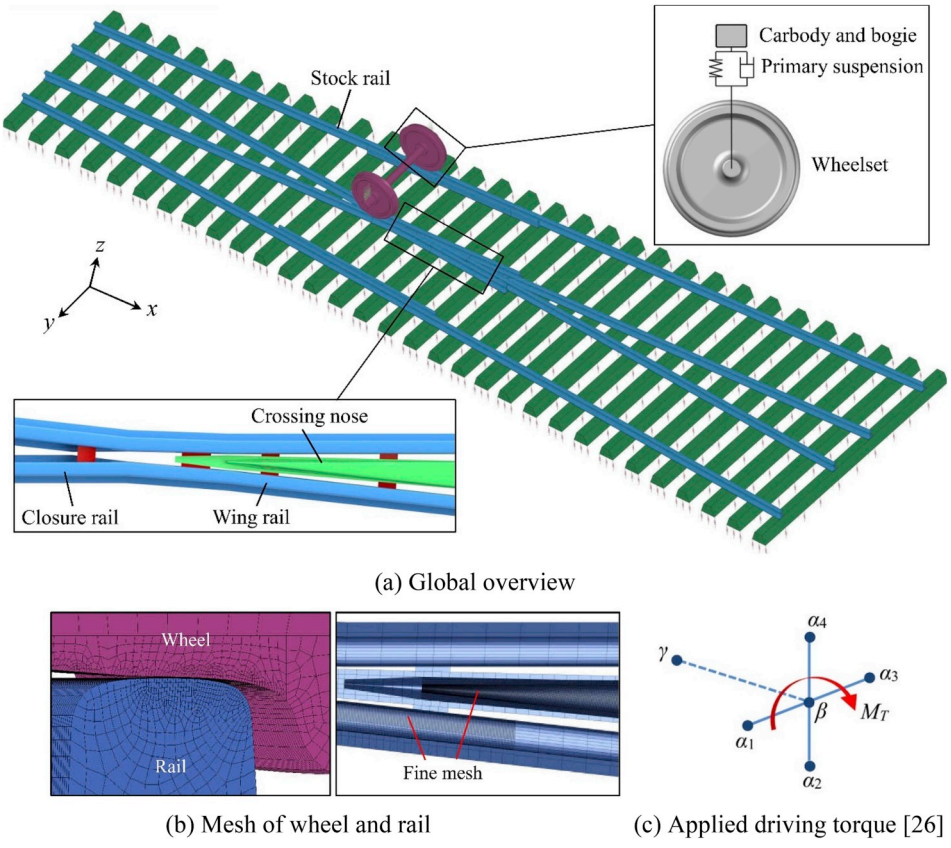

Fig. 1. 3D FE model for wheel/rail interaction at crossing.

case study on identifying the proper yield strength of the rail steel for 54E1-1:9 crossing under a specified traffic condition. Finally, Section 5 draws the main conclusions and proposed topics for further research.

2. Degradation of wheels and crossing rails due to dynamic interactions

The passage of one wheelset over a crossing panel is simulated using the commercial code ANSYS/LS-DYNA. The wheel/rail contact parameters obtained are then used to analyze wheel/rail degradation in terms of yield behavior, RCF and wear.

2.1. Dynamic wheel/rail interaction at crossing

Generally, the FE method is able to simulate the dynamic wheel/crossing interaction and related wheel/rail contact behavior for various types of crossings. In this study, a 54E1-1:9-type crossing (with the UIC54 rail profile and a crossing angle of 1:9) is modeled, as the dynamic response extracted from the model has been verified with in-situ axle box acceleration measurements [22]. The FE modeling is divided into the following steps.

2.1.1. Geometry, material and mesh

The length of the crossing model is approximately 17.8 m, which includes 31 sleepers, as shown in Fig. 1(a). In this model, rails and sleepers are modeled using hexahedral solid elements with the types of SOLID185 in ANSYS and SOLID164 in LS-DYNA. Railpads and ballast are modeled as linear springs and viscous dampers with the types of COMBIN14 in ANSYS and COMBI165 in LS-DYNA. The parameters of the railpads and ballast are obtained from in-situ hammer tests on the Dutch railway [24]. The stiffness and damping for a standard railpad are 1560 MN/m and 67.5 kN/m respectively, while the corresponding values for the ballast under a standard concrete sleeper are 90 MN/m and 64 kN/m.

Regarding the passage of the wheelset, one wheel runs along the closure rail, the wing rail and then across the gap, impacting the crossing nose, while the other wheel moves along the stock rail, as shown in Fig. 1 (a). The wheelset is modeled using the same solid element types as rails, while both the car body and bogie are simplified as lumped mass (MASS21 in ANSYS and MASS166 in LS-DYNA) and supported on the wheel axle by linear springs and viscous dampers. The stiffness and damping of the primary suspension are 880 kN/m and 4000 N/m [25], respectively. In total, the FE model is composed of 541,087 elements and 666,426 nodes.

A bilinear kinematic hardening material model is used for the contact bodies. The density, Young's modulus, tangent modulus and Poisson's ratio of the wheel and rail are 7800 kg/m^3, 210 GPa, 21 GPa and 0.3, respectively. The sleepers are treated as linear elastic bodies, with the Young's modulus, density and Poisson's ratio of 38 GPa, 2480 kg/m^3 and 0.2, respectively.

The wheel/rail contact is defined by the penalty contact algorithm, which checks each slave node for penetration through the master surface. In this study, the wheel surface serves as the master surface while the rail surface serves as the slave surface, and the minimum element size is set to 1 × 1 mm at the wheel/rail interface (see Fig. 1(b)). The wheel/rail tangential contact is solved by Coulomb's friction law, and the friction coefficient μ is set to 0.4 for dry and clean wheel/rail contact [27].

2.1.2. Initial and boundary conditions

The FE simulation consists of an implicit integration scheme using ANSYS and an explicit integration scheme using LS-DYNA. In the implicit program, only gravity is specified for the system to obtain the static equilibrium of a wheelset standing still on a crossing. The nodal displacements serve as the initial nodal coordinates for the implicit-explicit sequential analysis of dynamic wheel-rail interaction. In the explicit program, the initial nodal velocities are prescribed on the carbody for forward translation, and on the wheelset for both rotation and translation. To eliminate disturbances from wave reflections at the boundaries, the FE model employs non-reflecting boundary conditions.

Apart from gravity, driving torque M_T is also specified on the axis of the wheelset. Since the hexahedral solid elements of the wheelset have only translational freedom, the Hughes-Liu beam elements (of type BEAM161 in LS-DYNA) are employed to take the torque [26], as shown in Fig. 1(c). Each beam element is composed of three nodes, i.e., α (α_1~α_4 for each element), β and γ. In total, four beam elements are involved, and all the nodes are shared with the wheel solid elements. The torque is then applied on a driven node β, and its direction is determined by the right-hand rule. The value of the torque is determined by the traction coefficient μ_T, expressed as

$$\mu_T = \frac{F_T}{F_N} < \mu \tag{1}$$

where F_N and F_T are the wheel/rail normal and tangential contact forces. In principle, the value of μ_T is smaller than the friction coefficient μ, so that frictional contact with partial slip can be represented. In this study, the value of μ_T is set to 0.15. Note that the value of the traction coefficient fluctuates slightly due to structural vibrations in the dynamic wheel-rail interaction.

A central difference integration method is used for the explicit scheme, and the integration time step is 0.9 times of the critical time step. The critical time step is determined by the smallest element size of the FE model, that is, a sound wave should not cross the smallest element within the critical time step. In the FE simulation, the integration time step is calculated by LS-DYNA and equals to 2.3×10^{-8} s.

2.1.3. Output and post-processing

In this study, one passage of a wheelset over a crossing is simulated. A typical simulation at 80 km/h takes approximately 21 h by using 4 cores of Intel Xeon Gold 5115 2.4 GHz CPU. During the period, the wheelset rolls 1228 mm along the crossing rails. Of the total length of the running band, 638 mm takes place on wing rail and 620 mm takes place on crossing nose, with an overlap of 30 mm due to two-point wheel/rail contact.

The kinematic and dynamic nodal results (e.g., nodal force and displacement) are calculated from the FE simulation. The output time step ΔT is set to 2×10^{-5}s, at which time the wheelset translates 0.44 mm with a speed of 80 km/h. Thereafter, these results are used to extract the wheel/rail contact parameters in terms of contact patch, adhesion-slip state, pressure, shear stress and micro-slip [26,28].

2.2. Wheel and rail degradation

In general, the service life of wheels and rails is determined by three major degradation types, namely plastic deformation, RCF and wear. They can be calculated from the simulated wheel/rail contact parameters.

Plastic deformation comes from high contact stresses. This study employs the von Mises yield criterion to Ref. [29] evaluate the yield behavior of contact bodies. In the literature, it has been demonstrated that the wheel/rail plastic deformation under one loading cycle shows trends similar to that under thousands of loading cycles [2,30,31]. Therefore, it is reasonable to qualitatively evaluate the effect of plastic deformation based on the analysis of one wheelset passage. With such an assumption, some deformation behavior occurring under cyclic loads, e.g., cyclic plastic hardening, may not be properly accounted for in this study. In future works, attempts will be made to introduce more realistic constitutive models of materials, employ more explicit degradation indices (e.g., equivalent plastic strain) and include cyclic wheel loads [32–35], so as to represent the plastic deformation of contact bodies more accurately. The von Mises stress σ_{vm} is expressed as:

$$\sigma_{vm}=\sqrt{\frac{1}{2}\left[\left(\sigma_{xx}-\sigma_{yy}\right)^2+\left(\sigma_{yy}-\sigma_{zz}\right)^2+\left(\sigma_{zz}-\sigma_{xx}\right)^2+6\left(\sigma_{xy}^2+\sigma_{yz}^2+\sigma_{zx}^2\right)\right]} \tag{2}$$

where σ_{xx}, σ_{yy} and σ_{zz} are the normal stresses, and σ_{xy}, σ_{yz} and σ_{zx} are the shear stresses.

In the literature, RCF is commonly analyzed using the energy dissipation method and the shakedown method. In the energy dissipation method, the RCF index is determined via extensive testing and calibration [36], and is currently limited to a few steel types. Further experiments for calibration are required for more generalized wheel/rail steel types. The shakedown method [37,38], however, is not restricted to certain wheel/rail steel types. Therefore, a surface fatigue index FI_{surf} based on the shakedown method is employed, expressed as:

$$FI_{\text{surf}}=\left|\frac{F_T}{F_N}\right|-\frac{k}{p_0} \tag{3}$$

where k is the yield strength in shear, and p_0 is the maximum pressure in the contact patch. Surface-initiated RCF will occur if $FI_{\text{surf}}>0$.

Wear is the removal of material from the wheel/rail interface. In this study, Archard's sliding method is used to analyze the distribution of wear. In the sliding method, the volume of wear depends on the sliding distance, normal contact force and hardness of the material [39]. The wear volume V_{wear} can be expressed as:

$$V_{\text{wear}}=k_s\frac{F_N d}{H} \tag{4}$$

where d is the sliding distance, and H is the material hardness. The wear coefficient k_s is obtained from the wear chart [40], see Fig. 2. In the literature, the wear chart is widely used for wear prediction, and has been demonstrated for several wheel and rail steel types [41,42]. In this work, it is assumed that this wear chart is also appropriate for the studied combination of wheel and rail materials. In future work, the wear chart can be calibrated via lab tests when the materials are available for sampling.

In the FE simulation, the wear depth Δz of the wheel/rail interface can be calculated as [12]:

$$\Delta z=\frac{k_s}{H}\int_0^T ps\,\mathrm{d}t=\frac{k_s}{H}\sum_{i=1}^{n}p_i s_i \Delta T \tag{5}$$

where p is the pressure, and s is the sliding velocity. ΔT is the time step for the output, T is the duration of wheel/rail contact at the node and equals to $n\Delta T$. In Equation (5), the output time step ΔT is explicitly employed and differs from Equation (2)~(3), because wear is a cumulative process and lasts during the passage of the wheelset, while only the maximum values of von Mises stress and fatigue index are needed to evaluate the yield behavior and RCF.

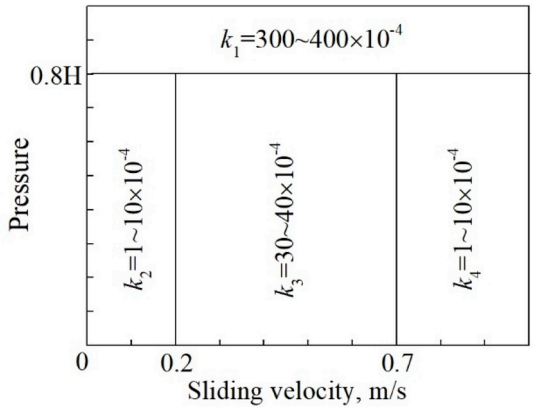

Fig. 2. Wear coefficient of Archard's model under dry conditions [40].

3. Multi-criteria evaluation of wheel/rail degradation behavior at crossings

It is a complicated process to analyze the integrated performance of wheels and crossing rails, not only because of the complex dynamics and different degradation types involved, but also due to the variations of parameter scenarios (e.g., train speed, axle load, wheel tread profile and friction coefficient) that can affect the wheel/rail degradation. This section proposes a multi-criteria method capable of evaluating the wheel/rail degradation behavior under various parameter scenarios; this method is divided into the following steps.

Step 1. Quantification of wheel/rail degradation

In real-life train operations, vehicles that run over a crossing often have inconstant traffic parameters, e.g., axle load, train speed, friction coefficient and wheel tread profile. Therefore, the evaluation of wheel/rail degradation behavior should account for the variation of traffic parameters. For demonstration purpose, the variation of three traffic parameters is analyzed, namely train speed, axle load and wheel yield strength. Each parameter scenario m can then be obtained by assembling the three traffic parameters, i.e., $\omega_m=[v_m, L_m, \sigma_{Y,m}^{\text{Wheel}}]^T$, where v_m is the train speed, L_m is the axle load and $\sigma_{Y,m}^{\text{Wheel}}$ is the wheel yield strength. The rest of the traffic parameters and conditions that could affect the wheel/rail degradation, e.g., the crossing type, friction coefficient and wheel tread profile, are held fixed for this evaluation. The fixed traffic parameters are included in the parameter θ, and their influence on wheel/rail degradation will be studied in further work.

Each scenario m will have a defined ratio ξ_m indicating its probability of occurring at the crossing. The ratio ξ_m is calculated by multiplying the ratio of each traffic parameter in the scenario, i.e., $\xi_m=\xi_m^v\cdot\xi_m^L\cdot\xi_m^\sigma$, where ξ_m^v is the ratio for a certain train speed over total traffics, ξ_m^L for a certain axle load and ξ_m^σ for a certain wheel yield strength.

For a variable λ to be evaluated (e.g., rail yield strength or crossing nose profile) in a parameter scenario m, the following objective functions can be defined to quantify the effect of yield behavior, RCF and wear:

$$J_{\text{Wheel}}^{\text{YB}}(\lambda,\theta,\omega_m)=\sum\nolimits_{n=1}^{N_{\text{Wheel}}}\delta\left(\sigma_{vm}^{\text{Wheel},n}(\lambda,\theta,\omega_m)-\sigma_Y^{\text{Wheel}}\right)\cdot\frac{\sigma_{vm}^{\text{Wheel},n}(\lambda,\theta,\omega_m)-\sigma_Y^{\text{Wheel}}}{\sigma_Y^{\text{Wheel}}}$$

$$J_{\text{Rail}}^{\text{YB}}(\lambda,\theta,\omega_m)=\sum\nolimits_{n=1}^{N_{\text{Rail}}}\delta\left(\sigma_{vm}^{\text{Rail},n}(\lambda,\theta,\omega_m)-\sigma_Y^{\text{Rail}}\right)\cdot\frac{\sigma_{vm}^{\text{Rail},n}(\lambda,\theta,\omega_m)-\sigma_Y^{\text{Rail}}}{\sigma_Y^{\text{Rail}}}$$

$$J_{\text{Wheel}}^{\text{RCF}}(\lambda,\theta,\omega_m)=\sum\nolimits_{n=1}^{N_{\text{Wheel}}}\delta\left(FI_{\text{surf}}^{\text{Wheel},n}(\lambda,\theta,\omega_m)\right)\cdot FI_{\text{surf}}^{\text{Wheel},n}(\lambda,\theta,\omega_m)$$

$$J_{\text{Rail}}^{\text{RCF}}(\lambda,\theta,\omega_m)=\sum\nolimits_{n=1}^{N_{\text{Rail}}}\delta\left(FI_{\text{surf}}^{\text{Rail},n}(\lambda,\theta,\omega_m)\right)\cdot FI_{\text{surf}}^{\text{Rail},n}(\lambda,\theta,\omega_m)$$

$$J_{\text{Wheel}}^{\text{W}}(\lambda,\theta,\omega_m)=\sum\nolimits_{n=1}^{N_{\text{Wheel}}}\Delta z^{\text{Wheel},n}(\lambda,\theta,\omega_m)$$

$$J_{\text{Rail}}^{\text{W}}(\lambda,\theta,\omega_m)=\sum\nolimits_{n=1}^{N_{\text{Rail}}}\Delta z^{\text{Rail},n}(\lambda,\theta,\omega_m)$$

$$\delta(x)=\begin{cases}0 & \text{if } x<0\\ 1 & \text{if } x\geq 0\end{cases} \tag{6}$$

where $J_{\text{Wheel}}^{\text{YB}}$ and $J_{\text{Rail}}^{\text{YB}}$ are the objective functions for characterizing the yield behavior of the wheel and rail, $J_{\text{Wheel}}^{\text{RCF}}$ and $J_{\text{Rail}}^{\text{RCF}}$ for RCF, and $J_{\text{Wheel}}^{\text{W}}$ and $J_{\text{Rail}}^{\text{W}}$ for wear. The binary function $\delta(x)\in\{0,1\}$ allows the inclusion in the sums of the terms that satisfy the condition given by x. N_{Wheel} and N_{Rail} are the total number of node/element of the wheel tread and rail head. $\sigma_{vm}^{\text{Wheel},n}$ and $\sigma_{vm}^{\text{Rail},n}$ are the von Mises stresses at element n of the wheel and rail, calculated using Equation (2). $FI_{\text{surf}}^{\text{Wheel},n}$ and $FI_{\text{surf}}^{\text{Rail},n}$ are the fatigue indices at element n of the wheel and rail, calculated using

Equation (3). Finally, $\Delta z^{\text{Wheel},\,n}$ and $\Delta z^{\text{Rail},\,n}$ are the wear depths at node n of the wheel and rail, calculated using Equation (5).

Thereafter, the confidence interval for each degradation type can be obtained, to characterize the complete range of possible degradation values. For instance, for an evaluation variable λ and fixed parameter θ, the interval $\left[\underline{J}^{\text{YB}}_{\text{Wheel}}(\lambda,\theta),\overline{J}^{\text{YB}}_{\text{Wheel}}(\lambda,\theta)\right]$ represents the range in which yield behavior of the wheel will vary within all the parameter scenarios.

$$\begin{aligned}\underline{J}^{\text{YB}}_{\text{Wheel}}(\lambda,\theta)&=\min_{m}\left\{J^{\text{YB}}_{\text{Wheel}}(\lambda,\theta,\omega_m)\right\}\\ \overline{J}^{\text{YB}}_{\text{Wheel}}(\lambda,\theta)&=\max_{m}\left\{J^{\text{YB}}_{\text{Wheel}}(\lambda,\theta,\omega_m)\right\}\end{aligned}\tag{7}$$

Step 2. Wheel/rail degradation under a specified traffic condition

Under a specified traffic condition, i.e., a certain combination of parameter scenarios, the estimated wheel/rail degradation indices for an evaluation variable λ can be calculated as:

$$\begin{aligned}\widehat{J}^{\text{YB}}_{\text{Wheel}}(\lambda,\theta)&=\sum\nolimits_{m=1}^{M}\overline{\xi}_m J^{\text{YB}}_{\text{Wheel}}(\lambda,\theta,\omega_m)\\ \widehat{J}^{\text{YB}}_{\text{Rail}}(\lambda,\theta)&=\sum\nolimits_{m=1}^{M}\overline{\xi}_m J^{\text{YB}}_{\text{Rail}}(\lambda,\theta,\omega_m)\\ \widehat{J}^{\text{RCF}}_{\text{Wheel}}(\lambda,\theta)&=\sum\nolimits_{m=1}^{M}\overline{\xi}_m J^{\text{RCF}}_{\text{Wheel}}(\lambda,\theta,\omega_m)\\ \widehat{J}^{\text{RCF}}_{\text{Rail}}(\lambda,\theta)&=\sum\nolimits_{m=1}^{M}\overline{\xi}_m J^{\text{RCF}}_{\text{Rail}}(\lambda,\theta,\omega_m)\\ \widehat{J}^{\text{W}}_{\text{Wheel}}(\lambda,\theta)&=\sum\nolimits_{m=1}^{M}\overline{\xi}_m J^{\text{W}}_{\text{Wheel}}(\lambda,\theta,\omega_m)\\ \widehat{J}^{\text{W}}_{\text{Rail}}(\lambda,\theta)&=\sum\nolimits_{m=1}^{M}\overline{\xi}_m J^{\text{W}}_{\text{Rail}}(\lambda,\theta,\omega_m)\end{aligned}\tag{8}$$

where M is the number of scenarios considered and $\overline{\xi}_m$ is the normalized ratio of scenario m, $\overline{\xi}_m=\xi_m/\sum_{m=1}^{M}\xi_m$. In this step, the objective function (7) is obtained for a range of evaluation variable λ, and its effect on the different degradation types can be analyzed.

Step 3. Degradation behavior of wheel/rail at crossings

To analyze the integrated effect of yield behavior, RCF and wear on wheel/rail degradation, the indices of the three degradation types are combined via:

$$\begin{aligned}J_{\text{Wheel}}(\lambda,\theta)&=\eta_{\text{YB}}\widehat{J}^{\text{YB}}_{\text{Wheel}}(\lambda,\theta)+\eta_{\text{RCF}}\widehat{J}^{\text{RCF}}_{\text{Wheel}}(\lambda,\theta)+\eta_{\text{W}}\widehat{J}^{\text{W}}_{\text{Wheel}}(\lambda,\theta)\\ J_{\text{Rail}}(\lambda,\theta)&=\eta_{\text{YB}}\widehat{J}^{\text{YB}}_{\text{Rail}}(\lambda,\theta)+\eta_{\text{RCF}}\widehat{J}^{\text{RCF}}_{\text{Rail}}(\lambda,\theta)+\eta_{\text{W}}\widehat{J}^{\text{W}}_{\text{Rail}}(\lambda,\theta)\end{aligned}\tag{9}$$

where $\eta_{\text{YB}}\geq 0$, $\eta_{\text{RCF}}\geq 0$, and $\eta_{\text{W}}\geq 0$ are the weight coefficients for each degradation type and satisfy $\eta_{\text{YB}}+\eta_{\text{RCF}}+\eta_{\text{W}}=1$. The selection of the weight coefficient is specified by the relative importance of each degradation type for the crossing.

Consequently, the wheel/rail degradation indices from Equation (9) are normalized and the index of wheel/rail degradation behavior (WRD) is defined as:

$$\begin{aligned}J^{\text{WRD}}_{\text{Wheel}}(\lambda,\theta)&=\frac{J_{\text{Wheel}}(\lambda,\theta)-\min_{\lambda}\{J_{\text{Wheel}}(\lambda,\theta)\}}{\max_{\lambda}\{J_{\text{Wheel}}(\lambda,\theta)\}-\min_{\lambda}\{J_{\text{Wheel}}(\lambda,\theta)\}}\\ J^{\text{WRD}}_{\text{Rail}}(\lambda,\theta)&=\frac{J_{\text{Rail}}(\lambda,\theta)-\min_{\lambda}\{J_{\text{Rail}}(\lambda,\theta)\}}{\max_{\lambda}\{J_{\text{Rail}}(\lambda,\theta)\}-\min_{\lambda}\{J_{\text{Rail}}(\lambda,\theta)\}}\end{aligned}\tag{10}$$

Finally, the following multi-criteria evaluation problem is solved to identify the trade-off between the wheel and rail degradations with an evaluation variable λ:

$$\min_{\lambda}\left\{J^{\text{WRD}}_{\text{Wheel}}(\lambda,\theta),J^{\text{WRD}}_{\text{Rail}}(\lambda,\theta)\right\}\tag{11}$$

The solution of this problem is called Pareto-optimal set X_{Pareto}. A solution x_{Pareto} belongs to the set X_{Pareto} if there does not exist another feasible solution λ such that:

(1) $J^{\text{WRD}}_{\text{Wheel}}(\lambda,\theta)\leq J^{\text{WRD}}_{\text{Wheel}}(x_{\text{Pareto}},\theta)$

(2) $J^{\text{WRD}}_{\text{Rail}}(\lambda,\theta)\leq J^{\text{WRD}}_{\text{Rail}}(x_{\text{Pareto}},\theta)$

(3) $J^{\text{WRD}}_{\text{Wheel}}(\lambda,\theta)<J^{\text{WRD}}_{\text{Wheel}}(x_{\text{Pareto}},\theta)$ or $J^{\text{WRD}}_{\text{Rail}}(\lambda,\theta)<J^{\text{WRD}}_{\text{Rail}}(x_{\text{Pareto}},\theta)$

Pareto front is the set of objective function values when evaluating the Pareto-optimal set, defined as $P_{\text{F}}=\left\{\left[J^{\text{WRD}}_{\text{Wheel}}(\lambda,\theta),J^{\text{WRD}}_{\text{Rail}}(\lambda,\theta)\right]^{T}:\lambda\in X_{\text{Pareto}}\right\}$. The information of the Pareto front can be used by infrastructure managers to determine their preferred variable for the traffic condition under consideration. If the infrastructure manager prefers to minimize the WRD index of the rail, or the WRD index of the wheel, or to find a compromise between them, the Pareto front will clearly indicate the trade-off and the compromise in performance when improving one of the indices.

A flowchart showing the multi-criteria evaluation method is presented in Fig. 3.

4. Case study: identifying optimized rail yield strength under a specified traffic condition

The multi-criteria evaluation method proposed in Section 3 is applied to identify the optimized rail yield strength for a 54E1-1:9 crossing under a specified traffic condition. Table 1 lists the parameter scenarios taken into account in the case study. In the case study, the rail yield strength ranges from 300 MPa to 1500 MPa, while the values of the Young's modulus and the tangent modulus remain unchanged. The preceding material properties may not exactly correspond to the rail steel types that have been in use, mainly due to the following considerations. First, the proposed method can be more easily demonstrated by tuning one variable while keeping other parameters fixed, and the influence of the variable on wheel/rail degradation can be more clearly observed. Second, the results obtained from this study can serve as a guide for selecting proper rail steel, improving existing rail steel (e.g., via heating, prestressing and explosion hardening), or developing new rail steel. Thus, the case study is not limited to existing rail steel types. In further work, the evaluation method will be improved to include more

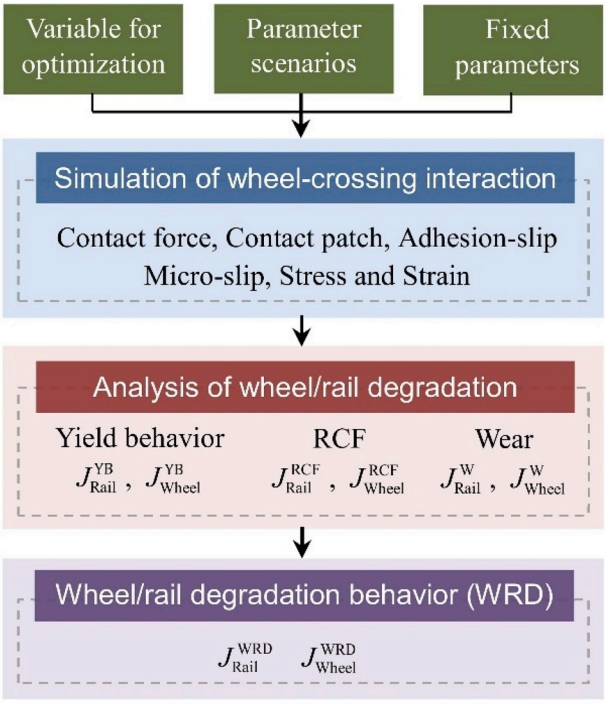

Fig. 3. Multi-criteria evaluation method for wheel/rail degradation behavior at crossings.

Table 1
Parameter scenarios for case study.

Scenario m	Train speed v (km/h)	Axle load L (t)	Wheel material σ_Y^{Wheel} (MPa)
1	80	16	500
2	40	16	500
3	120	16	500
4	80	20	500
5	80	24	500
6	80	16	700

variables and more efficient FE schemes, so that more realistic wheel/rail degradation behavior can be investigated in an efficient way.

4.1. From wheel/rail contact to degradation

The wheel/rail contact parameters in terms of contact force, contact patch, adhesion-slip state, pressure, shear stress and micro-slip are obtained from the FE simulation. Thereafter, these parameters are used to calculate the degradation of the wheel and crossing nose in terms of yield behavior, RCF and wear. Fig. 4 shows the distributions of contact parameters in Scenario 1 (see Table 1), in which v, L and σ_Y^{Wheel} equal 80 km/h, 16 t, and 500 MPa, respectively. The variable to be evaluated, i.e., rail yield strength σ_Y^{Rail}, is set to 300 MPa for demonstration purpose.

As shown in Fig. 4, the wheel starts to impact the crossing nose at $x = 231$ mm, from which the wheel/rail contact stays in the two-point contact stage until the wheel loses its contact with the wing rail at $x = 261$ mm. During this stage, the rolling radii differ between the two contact patches, which increase the magnitude of micro-slip and the proportion of slip region in the contact patch, contributing to the significant wear typically observed at that location of the crossing. Shortly after the two-point contact, both the normal and tangential contact forces reach their maxima, so that the shear stress in Patch 2 has higher magnitude than those in Patches 4 and 6.

Table 2 summarizes the maximum von Mises stress in Scenario 1. In each element, the highest value of the von Mises stress occurring as the wheelset passes is evaluated and plotted as the color contours in the table. The solid lines enclose the region where the maximum von Mises stress exceeds the yield strength. In Equation (6), only the regions enclosed by the solid lines are used to calculate the degradation index.

As shown in Table 2, the magnitude of von Mises stress ($\sigma_{vm}^{\text{Wheel}}$ and $\sigma_{vm}^{\text{Rail}}$) increases with the growth of σ_Y^{Rail} on both the wheel and rail. On the rail, the growth of $\sigma_{vm}^{\text{Rail}}$ is not as significant as σ_Y^{Rail}, so that the region with yield behavior shrinks on harder rail material, and there is almost no yield region at $\sigma_Y^{\text{Rail}} = 1500$ MPa. On the wheel, the region with yield behavior enlarges with the increase of σ_Y^{Rail} from 300 to 500 MPa, due to the usage of harder rail material; as the value of σ_Y^{Rail} reaches 500 MPa and higher, the magnitude of $\sigma_{vm}^{\text{Wheel}}$ grows monotonously, and yield of the wheel can take place within the almost whole running band.

Table 3 lists the distribution of RCF in Scenario 1. In all the simulated cases, RCF has a higher likelihood of occurring shortly after the wheel impacts the crossing nose. This outcome is mainly attributed to the enlargement of wheel/rail contact force and stresses during the impact. On the rail, the region with potential RCF (i.e., $FI_{\text{surf}}^{\text{Rail}} > 0$) shrinks with the increase of σ_Y^{Rail}, due to the more significant increase of yield strength compared with contact stresses, see in Equation (3). As the rail becomes even harder (i.e., $\sigma_Y^{\text{Rail}} \geq 1300$ MPa), $FI_{\text{surf}}^{\text{Rail}}$ is below zero throughout the rail, showing good RCF resistance. On the wheel, however, both the magnitude of $FI_{\text{surf}}^{\text{Wheel}}$ and the region with RCF increase with σ_Y^{Rail}, mainly

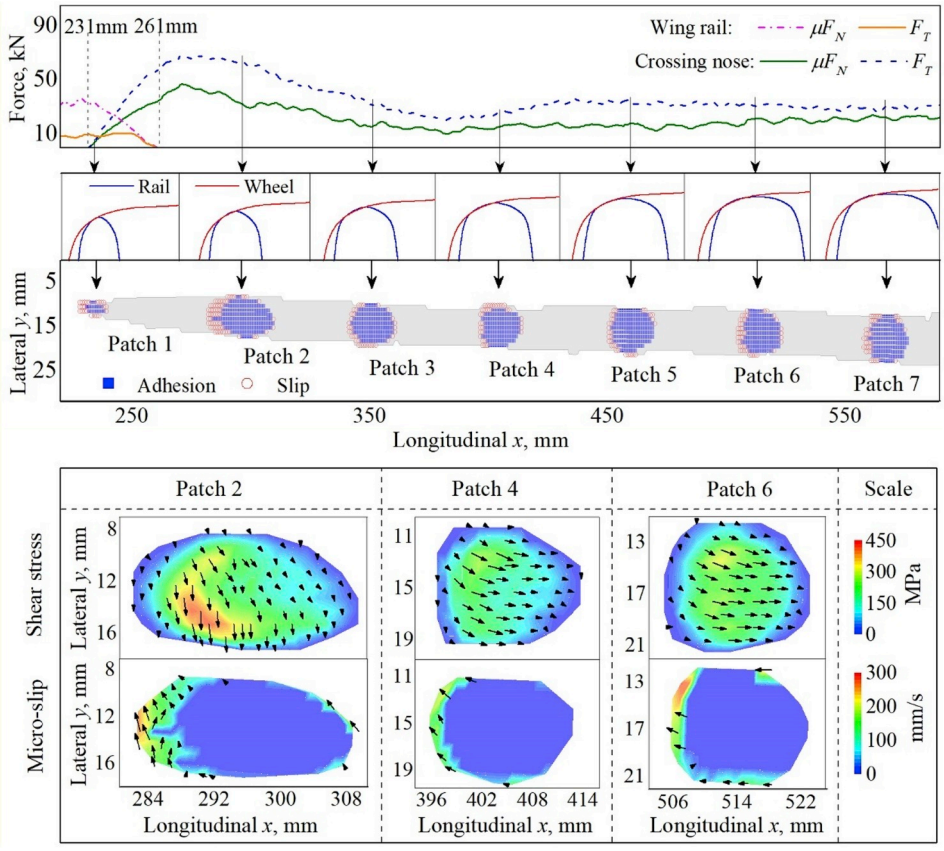

Fig. 4. Distribution of wheel/rail contact parameters with parameters $v = 80$ km/h, $L = 16$ t, $\sigma_Y^{\text{Wheel}} = 500$ MPa and $\sigma_Y^{\text{Rail}} = 300$ MPa. The first row is the normal/tangent contact force, the second row is the wheel/rail contact position, the third row is the running band, the fourth row is the field of surface shear stress and the fifth row is the field of micro-slip.

Table 2
Distribution of the highest von Mises stress occurring in each element during the wheelset passage, as indicated by the color contours. The results are obtained with scenario parameters $v = 80$ km/h, $L = 16$ t and $\sigma_Y^{\text{Wheel}} = 500$ MPa.

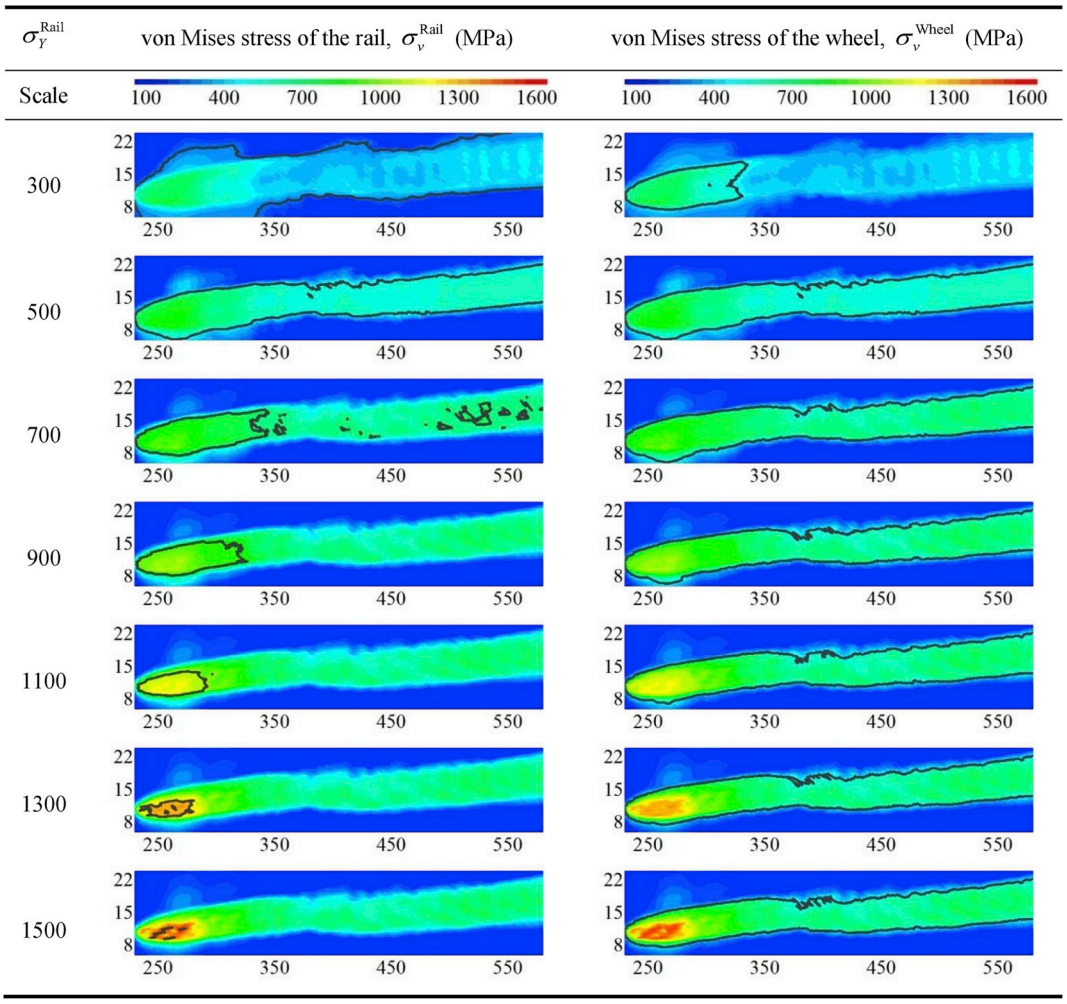

attributed to the fast growth of contact stresses, as illustrated in Table 2.

The wear of contact bodies is calculated using Equation (5), in which the hardness H is converted from the yield strength σ_Y via $H = (\sigma_Y + 90.7)/2.876$ [43]. Table 4 shows the distribution of wear in Scenario 1. In the table, the contours illustrate the accumulation of wear depth during one passage of the wheelset. In general, the growth of σ_Y^{Rail} exacerbates the wear of the wheel, which should be mainly attributed to the increase of contact stresses (see Table 2). On the rail, however, the magnitude of wear depth drops when σ_Y^{Rail} is higher, because the increase of the contact stresses is not as significant as the rail hardness (assumed to be proportional to σ_Y^{Rail}).

To quantify the wheel/rail degradation, the information shown in Tables 2–4 is processed via the objective function (i.e., Equation (6)), in which the variable σ_Y^{Rail} ranges from 300 MPa to 1500 MPa. Fig. 5 shows the wheel/rail degradation in Scenario 1. Generally, rail degradation is more sensitive to the variation of σ_Y^{Rail} than the wheel. With the increase of σ_Y^{Rail} from 300 to 1500 MPa, the values of $J_{\text{Rail}}^{\text{YB}}$, $J_{\text{Rail}}^{\text{RCF}}$ and $J_{\text{Rail}}^{\text{W}}$ decrease by 11.3, 1.2 and 5.6, which are 76%, 6% and 106% higher than $J_{\text{Wheel}}^{\text{YB}}$, $J_{\text{Wheel}}^{\text{RCF}}$ and $J_{\text{Wheel}}^{\text{W}}$ (i.e., 6.5, 1.1 and 2.7 respectively). In particular, both wheel and rail degradation change substantially with the increase of σ_Y^{Rail} from 300 to 700 MPa; as σ_Y^{Rail} reaches 900 MPa and higher, its influence on the wheel/rail degradation becomes less significant.

4.2. Influence of train speed

The dynamic wheel/crossing interaction in Scenarios 1–3 is simulated, in which a wheelset with the axle load L of 16 t runs over a crossing at different speeds v of 40, 80 and 120 km/h. Fig. 6 compares the wheel/rail degradation among these scenarios.

As shown in Fig. 6, an increase in train speed exacerbates wheel/rail degradation in terms of all the three types. In particular, wear is more sensitive to train speed than the other types. For example, the wear indices $J_{\text{Wheel}}^{\text{W}}$ and $J_{\text{Rail}}^{\text{W}}$ at 120 km/h increase by 447–738% compared with their values at 40 km/h. This phenomenon is mainly attributed to the following factors. First and most important, the wear coefficient is not constant and depends significantly on micro-slip velocity (see Fig. 2), so that the wear coefficient at 120 km/h is much higher than that at 40 km/h. Meanwhile, high train speed induces large impact force and contact stresses, which also contribute to high wear coefficient and thus fast wear.

The influence of train speed on yield behavior and RCF, however, is much less significant in comparison to wear. From 40 km/h to 120 km/h, the indices of yield behavior (i.e., $J_{\text{Wheel}}^{\text{YB}}$ and $J_{\text{Rail}}^{\text{YB}}$) and RCF (i.e., $J_{\text{Wheel}}^{\text{RCF}}$ and $J_{\text{Rail}}^{\text{RCF}}$) increase by 27–76% and 12–40%, due to the increase in wheel/rail impact force and contact stresses. Note that, both $J_{\text{Rail}}^{\text{YB}}$ and $J_{\text{Rail}}^{\text{RCF}}$ approach zero when σ_Y^{Rail} exceeds 700 MPa (i.e., 1.4 times of σ_Y^{Wheel}),

Table 3
Distribution of RCF with scenario parameters v = 80 km/h, L = 16 t and σ_Y^{Wheel} = 500 MPa.

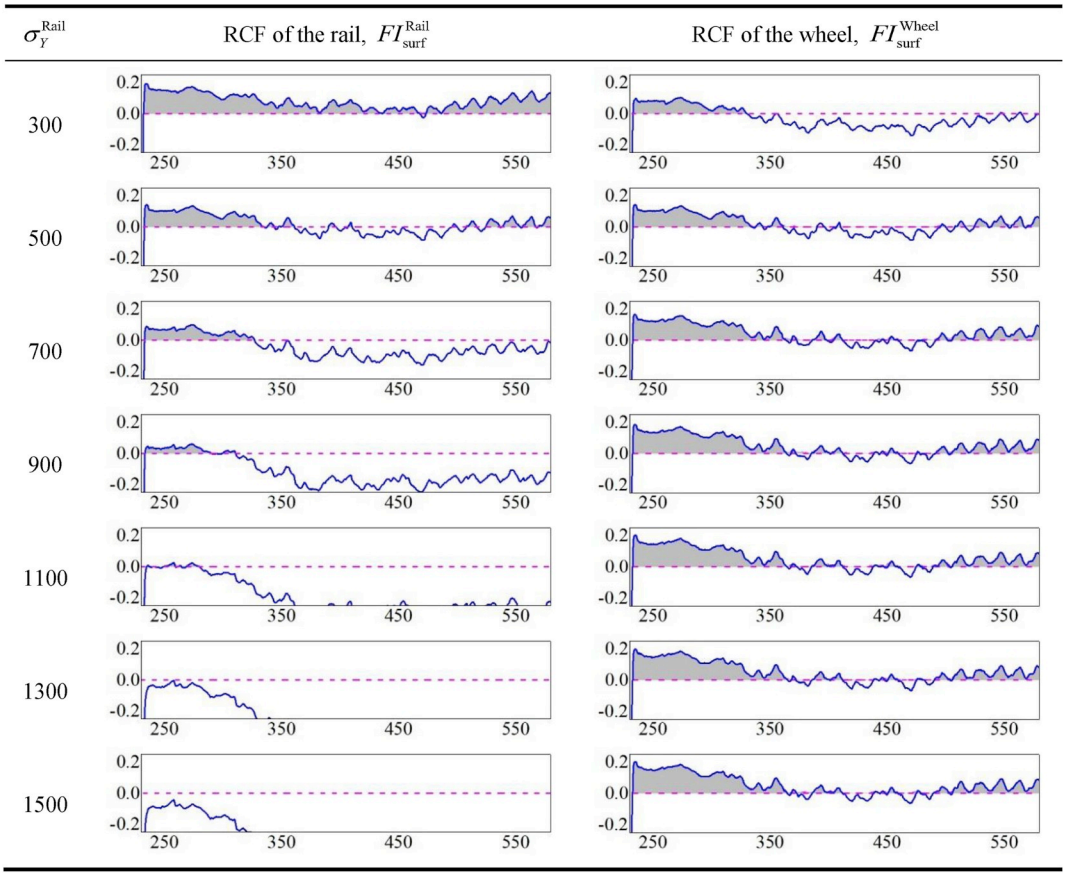

indicating that they are rarely affected by the train speed.

4.3. Influence of axle load

The dynamic wheel/crossing interaction in Scenarios 1, 4 and 5 is simulated, in which a wheelset with different axle loads L of 16, 20 and 24 t runs over a crossing at the same speed v of 80 km/h. Fig. 7 compares the wheel/rail degradation between the three scenarios. As shown in Fig. 7, the values of $J_{\text{Wheel}}^{\text{YB}}$ and $J_{\text{Wheel}}^{\text{RCF}}$ with L = 24 t are 28–34% and 40–66% higher than the corresponding values with L = 16 t. On the rail, the values of $J_{\text{Rail}}^{\text{YB}}$ and $J_{\text{Rail}}^{\text{RCF}}$ also increase with axle load when $\sigma_Y^{\text{Rail}} \leq$ 700 MPa; as σ_Y^{Rail} exceeds 700 MPa (i.e., 1.4 times of σ_Y^{Wheel}), both $J_{\text{Rail}}^{\text{YB}}$ and $J_{\text{Rail}}^{\text{RCF}}$ approach zero, so that they become less dependent on the axle load.

The growth of the axle load also exacerbates the wear of contact bodies, yet its influence is not as significant as the train speed. A 50% increase in axle load (from 16 to 24 t) results in 20–59% growth of $J_{\text{Wheel}}^{\text{W}}$ and $J_{\text{Rail}}^{\text{W}}$, as shown in Fig. 7(c), while a 50% increase in the train speed (from 80 to 120 km/h) leads to an 86–120% and a 93–153% increase in $J_{\text{Wheel}}^{\text{W}}$ and $J_{\text{Rail}}^{\text{W}}$, respectively (see Fig. 6(c)). This outcome is because the wear coefficient is more sensitive to variations of train speed, as illustrated in Section 4.2.

4.4. Influence of wheel yield strength

The yield strength of commonly used wheel steels (e.g., R7E, R7T, R8E and R8T) are in the range of 420–800 MPa [44–46]. In this section, two values within this range, i.e., 500 and 700 MPa, are selected to demonstrate their influence on wheel/rail degradation. A natural extension of this study is to include other wheel material properties (e.g., the Young's modulus and tangent modulus) as traffic parameters.

The dynamic wheel/crossing interaction in Scenarios 1 and 6 is simulated, in which a wheelset with an axle load L of 16 t and different yield strengths σ_Y^{Wheel} of 500 and 700 MPa runs over a crossing at the train speed v of 80 km/h. Fig. 8 compares the wheel/rail degradation between the two scenarios. In the figure, the increase of σ_Y^{Wheel} significantly suppresses wheel degradation. For example, the values of $J_{\text{Wheel}}^{\text{YB}}$, $J_{\text{Wheel}}^{\text{RCF}}$ and $J_{\text{Wheel}}^{\text{W}}$ at σ_Y^{Wheel} = 700 MPa reduce by 62–76%, 46–75% and 23–29%, respectively, compared to the values at σ_Y^{Wheel} = 500 MPa. However, rail degradation exacerbates at higher σ_Y^{Wheel}, since the values of $J_{\text{Rail}}^{\text{YB}}$, $J_{\text{Rail}}^{\text{RCF}}$ and $J_{\text{Rail}}^{\text{W}}$ with σ_Y^{Wheel} = 700 MPa rise by 13–43%, 12–40% and 1–14%, respectively, compared to the values with σ_Y^{Wheel} = 500 MPa.

4.5. Wheel/rail degradation behavior under a specified traffic condition

This section investigates wheel/rail degradation behavior at a crossing, and the optimized rail yield strength is identified for the specified traffic conditions.

The passage of a wheelset over a 54E1-1:9 crossing is simulated using the FE method, and the resulting wheel/rail degradation is extracted via Equation (2)~(6). Fig. 9 shows the confidence interval of each degradation type in Scenarios 1–6 (see Table 1).

To demonstrate the multi-criteria evaluation method proposed in Section 3, a specified traffic condition is assumed by assembling various combinations of train speed, axle load and wheel yield strength. The

Table 4
Distribution of wear with scenario parameters $v = 80$ km/h, $L = 16$ t and $\sigma_Y^{\text{Wheel}} = 500$ MPa.

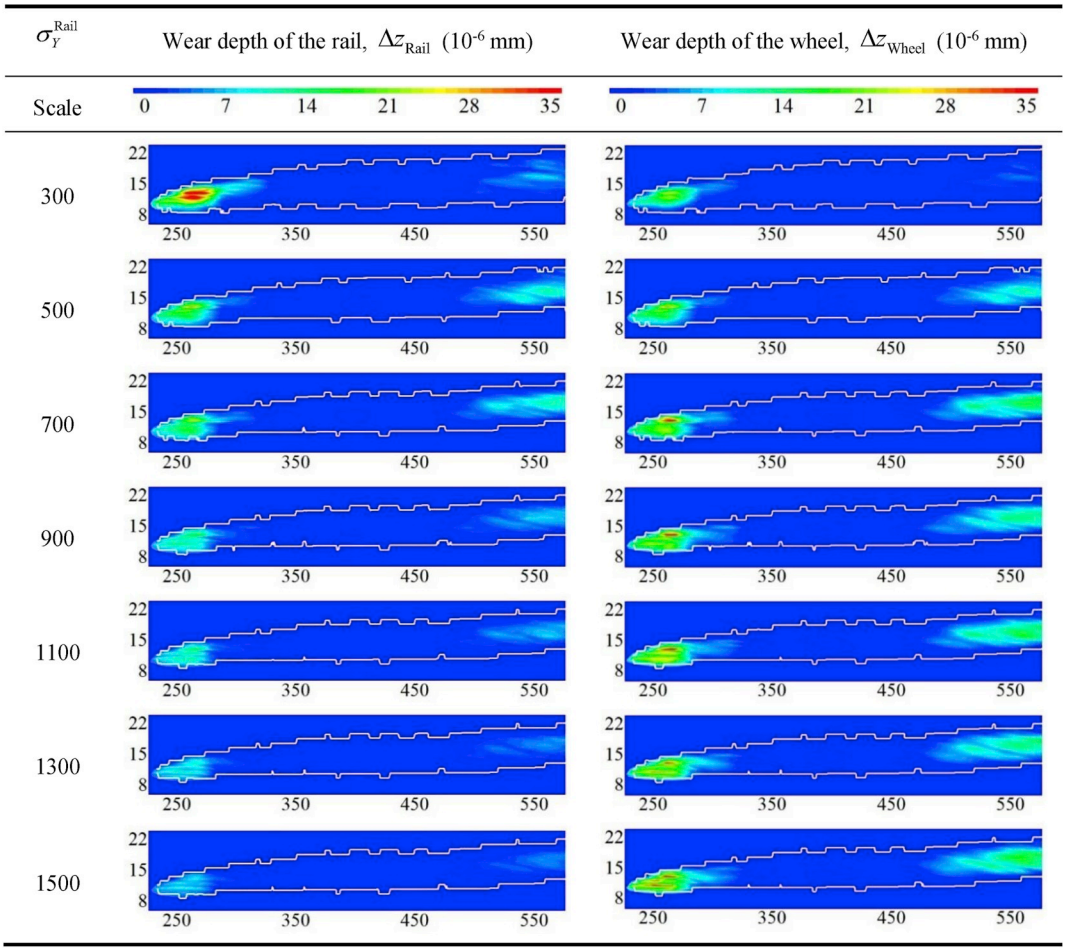

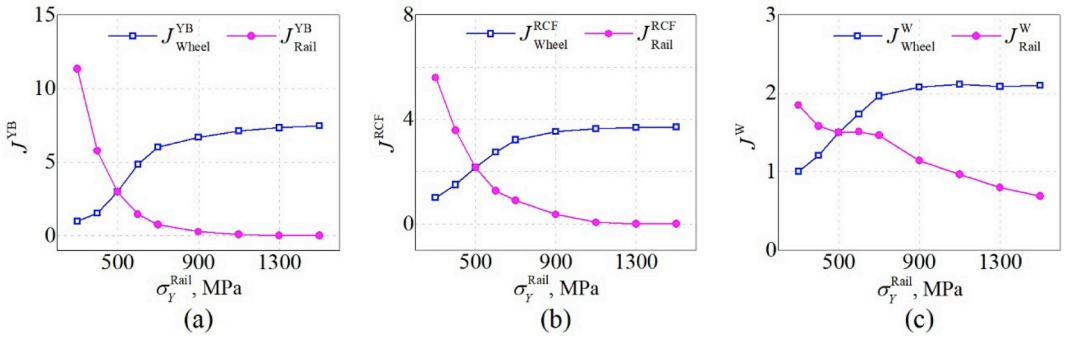

Fig. 5. Wheel/rail degradation with scenario parameters $v = 80$ km/h, $L = 16$ t and $\sigma_Y^{\text{Wheel}} = 500$ MPa. (a) Yield behavior, (b) RCF and (c) Wear.

ratio ξ of each scenario parameter over the total traffic is listed in Table 5. Further research could be done by tailoring the traffic to statistics of real-life conditions and including more generalized scenario parameters.

Under the specified traffic condition, the objective functions of wheel/rail degradation can then be calculated for Scenarios 1–6. Fig. 10 shows the distributions of wheel/rail degradation.

Thereafter, the information from Figs. 9 and 10 is combined to estimate the wheel/rail degradation indices via Equation (8). Fig. 11 illustrates the degradation indices of yield behavior, RCF and wear under the specified traffic condition.

Finally, the wheel/rail degradation behavior is evaluated using Equations (9)–(11). In Equation (10), a higher weight coefficient is specified for RCF (i.e., $\eta_{\text{RCF}} = 0.4$) compared with yield behavior (i.e., $\eta_{\text{YB}} = 0.3$) and wear (i.e., $\eta_{\text{W}} = 0.3$), because RCF may lead to the sudden failure of materials and is more dangerous to railway operations. Fig. 12 shows the Pareto front between the proposed WRD indices $J^{\text{WRD}}_{\text{Wheel}}(\sigma_Y^{\text{Rail}}, \theta)$ and $J^{\text{WRD}}_{\text{Rail}}(\sigma_Y^{\text{Rail}}, \theta)$.

Under the specified traffic condition, the following wheel/rail degradation behavior can be identified:

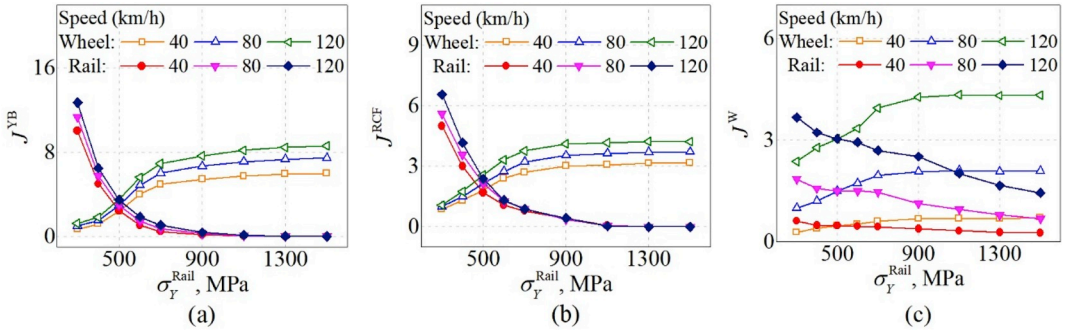

Fig. 6. Influence of train speed on wheel/rail degradation. (a) Yield behavior, (b) RCF and (c) Wear.

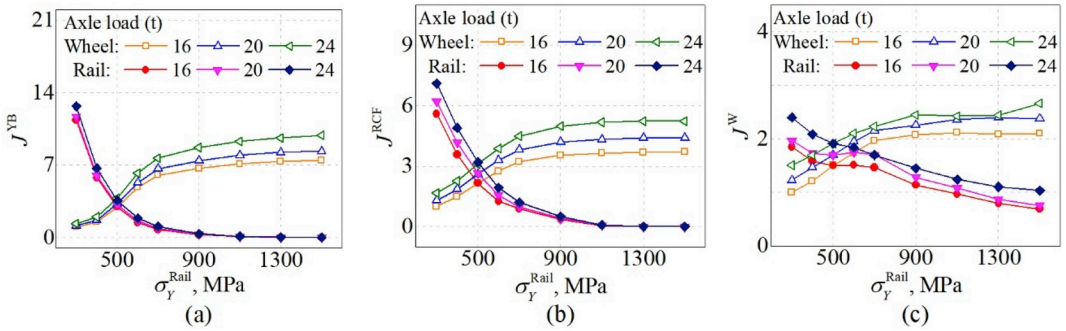

Fig. 7. Influence of axle load on wheel/rail degradation. (a) Yield behavior, (b) RCF and (c) Wear.

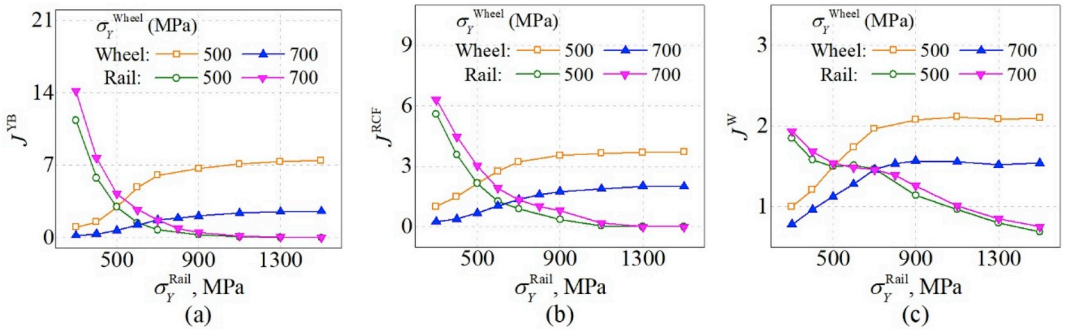

Fig. 8. Influence of wheel yield strength on wheel/rail degradation. (a) Yield behavior, (b) RCF and (c) Wear.

- 300 MPa $\leq \sigma_Y^{Rail} \leq$ 500 MPa (region in green color): the increase of σ_Y^{Rail} in this range exacerbates wheel degradation while reducing the rail degradation. In particular, J_{Rail}^{WRM} is more sensitive to the change of σ_Y^{Rail} compared to J_{Wheel}^{WRM}, so that the growth of σ_Y^{Rail} can significantly slow down rail degradation.
- 500 MPa $< \sigma_Y^{Rail} \leq$ 700 MPa (region in yellow color): the variation of σ_Y^{Rail} has a greater influence on J_{Wheel}^{WRM} than J_{Rail}^{WRM}. That is, the increase of σ_Y^{Rail} can significantly exacerbate wheel degradation, while its effect on suppressing rail degradation becomes less significant.
- 700 MPa $< \sigma_Y^{Rail} \leq$ 1500 MPa (region in pink color): the values of J_{Wheel}^{WRM} and J_{Rail}^{WRM} approach 1 and 0, respectively, which means neither wheel nor rail degradations change much with the variation of σ_Y^{Rail}.

The information demonstrated in Fig. 12 can be used by infrastructure managers to determine the crossing rail material for specified traffic conditions. If the major objective is to minimize rail degradation yet disregard wheel degradation, a rail satisfying $\sigma_Y^{Rail} >$ 700 MPa is appropriate; if the major objective is to minimize wheel degradation yet disregard rail degradation, the value of σ_Y^{Rail} should be lower than 500 MPa; if the effort is to achieve a trade-off between wheel and rail degradation, a rail satisfying 500 MPa $< \sigma_Y^{Rail} \leq$ 600 MPa can be used.

Note that the estimation of Pareto front is influenced by several factors. On one hand, various maintenance strategies may be specified by the infrastructure authorities based on the crossing types and traffic conditions, so that the weight coefficients η can be different. On the other hand, it is assumed that the wheel/rail contact is under dry and clean condition, whereas liquids may be present at the wheel/rail interface and introduce hydro-pressure, challenging the FE simulation. Moreover, the RCF index shown in Equation (3) corresponds to ratchetting and/or low-cycle fatigue [38], while the material behavior of wheels and rails in high-cycle loads needs to be analyzed in further work.

5. Conclusions and further works

This study aims to gain a better understanding of the integrated performance of wheels and rails at railway crossings. For this purpose, the dynamic wheel/crossing interaction is analyzed using a 3D explicit FE model, and the wheel/rail contact parameters serve as inputs for the

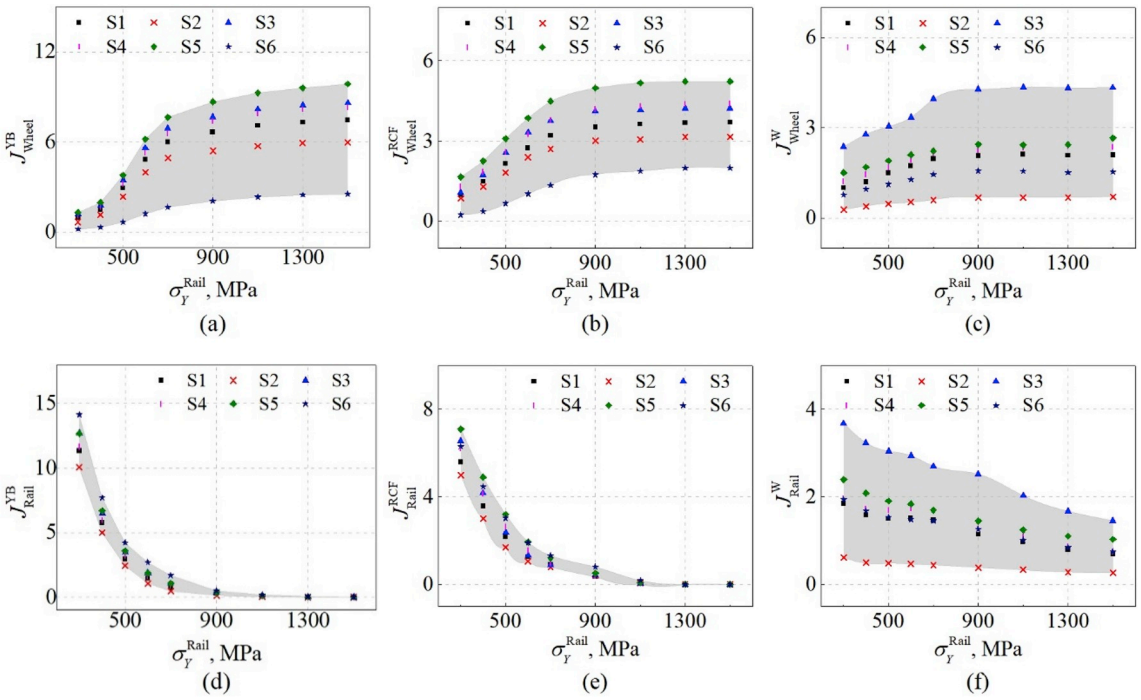

Fig. 9. Confidence interval of each degradation type.

Table 5
Ratio of scenario parameters.

Parameter	Value	Ratio ξ (%)
Train speed (km/h)	40	89.9
	80	10
	120	0.1
Axle load (t)	16	40
	20	40
	24	20
Wheel yield strength (MPa)	500	80
	700	20

multi-criteria evaluation of the integrated performance of wheels and crossing rails in terms of yield behavior, RCF and wear. By evaluating wheel/rail degradation under various scenarios, their degradation behavior can then be identified. The main conclusions are as follows:

- Increases of the train speed and axle load exacerbate wheel/rail degradation in terms of all the three types; in particular, wear of contact bodies is more sensitive to train speed compared with yield and RCF.
- An increase of the wheel yield strength suppresses wheel degradation while exacerbating rail degradation, and the phenomenon is converse for the growth of rail yield strength. Under the condition that the wheel yield strength equals to 500 MPa, yield and RCF have a low likelihood to presence on crossing rails when the rail yield strength exceeds 700 MPa.

The multi-criteria evaluation method is demonstrated via a case study, in order to identify the optimized rail yield strength for a 54E1-1:9 crossing under a specified traffic condition. The case study indicates that a rail with yield strength above 700 MPa is appropriate if the major objective is to minimize rail degradation while disregarding wheel degradation; if the major objective is to minimize wheel degradation yet disregarding rail degradation, the rail yield strength should be lower than 500 MPa; if the goal is to achieve a trade-off of wheel/rail degradation, the rail yield strength in the range of 500–600 MPa is preferred.

In further work, the degradation behavior between the wheel and crossing rail will be analyzed for more generalized scenarios, accounting

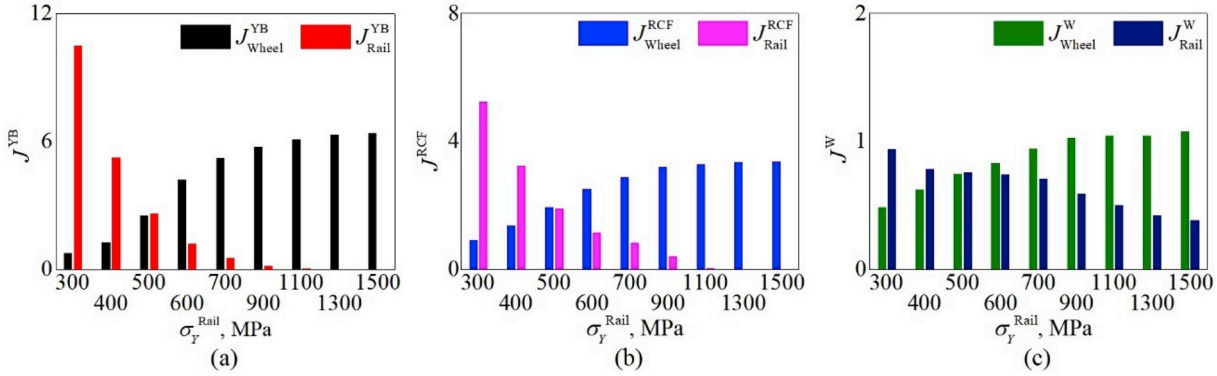

Fig. 10. Summary of wheel/rail degradation under the specified traffic condition. (a) Yield behavior, (b) RCF and (c) Wear.

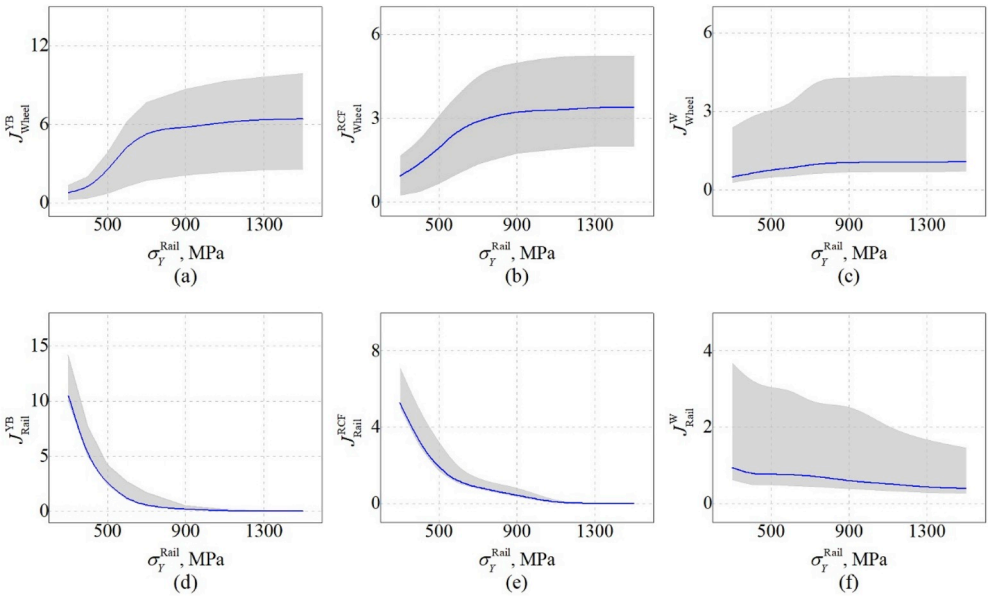

Fig. 11. Wheel/rail degradation under the specified traffic condition.

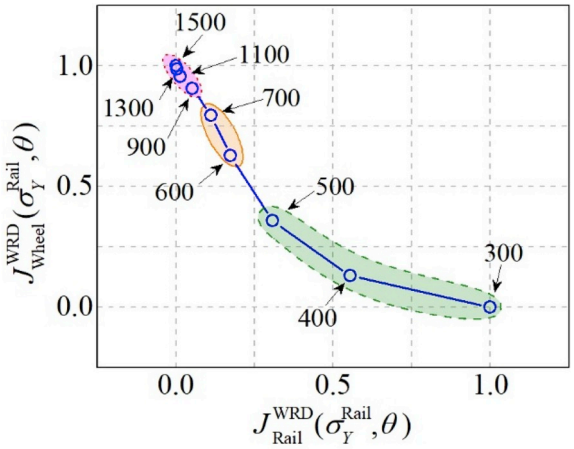

Fig. 12. Pareto front of the WRD index under the specified traffic condition. The dots and arrows indicate the values of σ_Y^{Rail}. 80% of the total traffics is with the wheel yield strength σ_Y^{Wheel} = 500 MPa, while the rest is with σ_Y^{Wheel} = 700 MPa.

for variations of friction coefficient, wheel profile, and crossing type among other variables that were assumed to be fixed in this study. In addition, the objective function proposed in this study focuses on wheel/rail degradation at crossings, and it can be extended to other weak points of the railway track, such as insulted joints and welds.

Author statement

Zilong Wei: Data curation; Formal analysis; Investigation; Methodology; Software; Validation; Visualization; Roles/Writing - original draft; Writing - review & editing. Alfredo Nunez: Formal analysis; Methodology; Supervision; Roles/Writing - original draft; Writing - review & editing. Xiubo Liu: Formal analysis; Funding acquisition; Project administration; Resources; Supervision; Writing - review & editing. Rolf Dollevoet: Conceptualization; Funding acquisition; Project administration; Resources; Supervision; Writing - review & editing. Zili Li: Conceptualization; Formal analysis; Funding acquisition; Methodology; Project administration; Resources; Supervision; Roles/Writing - original draft; Writing - review & editing.

Declaration of competing interest

We have no conflicts of interest to disclose.

Acknowledgements

The first author is partly supported by the Scientific Research Plan of China Railway No. K2019G010 as well as the Science and Technology Research Plan of China Academy of Railway Sciences No. 2018YJ146.

References

[1] Pålsson BA. Optimisation of railway crossing geometry considering a representative set of wheel profiles. Veh Syst Dyn 2015;53:274–301.
[2] Wiest M, Daves W, Fischer F, Ossberger H. Deformation and damage of a crossing nose due to wheel passages. Wear 2008;265:1431–8.
[3] Nicklisch D, Kassa E, Nielsen J, Ekh M, Iwnicki S. Geometry and stiffness optimization for switches and crossings, and simulation of material degradation. Proc Inst Mech Eng - Part F J Rail Rapid Transit 2010;224:279–92.
[4] Lagos RF, Alonso A, Vinolas J, Pérez X. Rail vehicle passing through a turnout: analysis of different turnout designs and wheel profiles. Proc Inst Mech Eng - Part F J Rail Rapid Transit 2012;226:587–602.
[5] Zhou Y, Wang S, Wang T. Field and laboratory investigation of the relationship between rail head check and wear in a heavy-haul railway. Wear 2014;315:68–77.
[6] Xin L, Markine V, Shevtsov I. Analysis of the effect of repair welding/grinding on the performance of railway crossings using field measurements and finite element modeling. Proc Inst Mech Eng - Part F J Rail Rapid Transit 2018;232:798–815.
[7] Sae Siew J, Mirza O, Kaewunruen S. Torsional effect on track-support structures of railway turnouts crossing impact. J Transport Eng, Part A: Systems 2016;143:06016001.
[8] Vu M, Kaewunruen S, Attard M. Nonlinear 3D finite-element modeling for structural failure analysis of concrete sleepers/bearers at an urban turnout diamond. Handbook of materials failure analysis with case studies from the chemicals, concrete and power industries. Elsevier; 2016. p. 123–60.
[9] Pletz M, Daves W, Ossberger H. A wheel passing a crossing nose: dynamic analysis under high axle loads using finite element modelling. Proc Inst Mech Eng - Part F J Rail Rapid Transit 2012;226:603–11.
[10] Guo S, Sun D, Zhang F, Feng X, Qian L. Damage of a Hadfield steel crossing due to wheel rolling impact passages. Wear 2013;305:267–73.
[11] Wan C, Markine V, Shevtsov I. Optimisation of the elastic track properties of turnout crossings. Proc Inst Mech Eng - Part F J Rail Rapid Transit 2014;230:360–73.
[12] Eadie DT, Elvidge D, Oldknow K, Stock R, Pointner P, Kalousek J, et al. The effects of top of rail friction modifier on wear and rolling contact fatigue: full-scale rail–wheel test rig evaluation, analysis and modelling. Wear 2008;265:1222–30.
[13] Eadie D, Santoro M. Top-of-rail friction control for curve noise mitigation and corrugation rate reduction. J Sound Vib 2006;293:747–57.
[14] Matsumoto A, Sato Y, Ohno H, Tomeoka M, Matsumoto K, Ogino T, et al. Improvement of bogie curving performance by using friction modifier to rail/wheel interface: verification by full-scale rolling stand test. Wear 2005;258:1201–8.

[15] Wan C, Markine V, Shevtsov I. Optimisation of the elastic track properties of turnout crossings. Proc Inst Mech Eng - Part F J Rail Rapid Transit 2016;230:360–73.
[16] Ayasse JB, Chollet H. Determination of the wheel rail contact patch in semi-Hertzian conditions. Veh Syst Dyn 2005;43:161–72.
[17] Piotrowski J, Chollet H. Wheel–rail contact models for vehicle system dynamics including multi-point contact. Veh Syst Dyn 2005;43:455–83.
[18] Quost X, Sebes M, Eddhahak A, Ayasse J-B, Chollet H, Gautier P-E, et al. Assessment of a semi-Hertzian method for determination of wheel–rail contact patch. Veh Syst Dyn 2006;44:789–814.
[19] Kalker JJ. A fast algorithm for the simplified theory of rolling contact. Veh Syst Dyn 1982;11:1–13.
[20] Burgelman N, Li Z, Dollevoet R. A new rolling contact method applied to conformal contact and the train–turnout interaction. Wear 2014;321:94–105.
[21] Blanco-Lorenzo J, Santamaria J, Vadillo EG, Correa N. On the influence of conformity on wheel–rail rolling contact mechanics. Tribol Int 2016;103:647–67.
[22] Wei Z, Shen C, Li Z, Dollevoet R. Wheel–rail impact at crossings: relating dynamic frictional contact to degradation. J Comput Nonlinear Dyn 2017;12:041016.
[23] Wei Z, Núñez A, Boogaard A, Dollevoet R, Li Z. Method for evaluating the performance of railway crossing rails after long-term service. Tribol Int 2018;123:337–48.
[24] Oregui M, Li Z, Dollevoet R. An investigation into the modeling of railway fastening. Int J Mech Sci 2015;92:1–11.
[25] Zhao X, Li Z, Liu J. Wheel–rail impact and the dynamic forces at discrete supports of rails in the presence of singular rail surface defects. Proc Inst Mech Eng - Part F J Rail Rapid Transit 2012;226:124–39.
[26] Yang Z, Deng X, Li Z. Numerical modeling of dynamic frictional rolling contact with an explicit finite element method. Tribol Int 2019;129:214–31.
[27] Areiza Y, Garcés S, Santa J, Vargas G, Toro A. Field measurement of coefficient of friction in rails using a hand-pushed tribometer. Tribol Int 2015;82:274–9.
[28] Zhao X, Li Z. The solution of frictional wheel–rail rolling contact with a 3D transient finite element model: validation and error analysis. Wear 2011;271:444–52.
[29] Mises Rv. Mechanik der festen Körper im plastisch-deformablen Zustand. Nachrichten von der Gesellschaft der Wissenschaften zu Göttingen. Mathematisch-Physikalische Klasse 1913;1913:582–92.
[30] Bandula-Heva T, Dhanasekar M. Failure of discontinuous railhead edges due to plastic strain accumulation. Eng Fail Anal 2014;44:110–24.
[31] Johansson A, Pålsson B, Ekh M, Nielsen JC, Ander MK, Brouzoulis J, et al. Simulation of wheel–rail contact and damage in switches & crossings. Wear 2011;271:472–81.
[32] Daves W, Kubin W, Scheriau S, Pletz M. A finite element model to simulate the physical mechanisms of wear and crack initiation in wheel/rail contact. Wear 2016;366:78–83.
[33] Wiedorn J, Daves W, Ossberger U, Ossberger H, Pletz M. Simplified explicit finite element model for the impact of a wheel on a crossing–validation and parameter study. Tribol Int 2017;111:254–64.
[34] Wiedorn J, Daves W, Ossberger U, Ossberger H, Pletz M. Numerical assessment of materials used in railway crossings by predicting damage initiation–Validation and application. Wear 2018;414:136–50.
[35] Pletz M, Meyer KA, Künstner D, Scheriau S, Daves W. Cyclic plastic deformation of rails in rolling/sliding contact–quasistatic FE calculations using different plasticity models. Wear 2019;436:202992.
[36] Burstow M. Whole life rail model application and development for RSSB–continued development of an RCF damage parameter. London: Rail Standards and Safety Board; 2004.
[37] Ekberg A, Kabo E. Fatigue of railway wheels and rails under rolling contact and thermal loading—an overview. Wear 2005;258:1288–300.
[38] Ekberg A, Kabo E, Andersson H. An engineering model for prediction of rolling contact fatigue of railway wheels. Fatigue Fract Eng Mater Struct 2002;25:899–909.
[39] Archard J, Hirst W. The wear of metals under unlubricated conditions. In: Proceedings of the Royal Society Of london A: mathematical, physical and engineering Sciences. The Royal Society; 1956. p. 397–410.
[40] Jendel T. Prediction of wheel profile wear—comparisons with field measurements. Wear 2002;253:89–99.
[41] Ramalho A, Esteves M, Marta P. Friction and wear behaviour of rolling–sliding steel contacts. Wear 2013;302:1468–80.
[42] Wang P, Xu J, Xie K, Chen R. Numerical simulation of rail profiles evolution in the switch panel of a railway turnout. Wear 2016;366–367:105–15.
[43] Pavlina E, Van Tyne C. Correlation of yield strength and tensile strength with hardness for steels. J Mater Eng Perform 2008;17:888–93.
[44] Jones R, Molent L, Walker K. Fatigue crack growth in a diverse range of materials. Int J Fatigue 2012;40:43–50.
[45] Tunna J, Sinclair J, Perez J. A Review of wheel wear and rolling contact fatigue. Proc Inst Mech Eng - Part F J Rail Rapid Transit 2007;221:271–89.
[46] Donzella G, Faccoli M, Mazzù A, Petrogalli C, Roberti R. Progressive damage assessment in the near-surface layer of railway wheel–rail couple under cyclic contact. Wear 2011;271:408–16.